

# Decoupling early-age free shrinkage and restraint effects in 3D printed concrete using Digital Image Correlation

Aniket Kumar Patel<sup>1</sup>, Avinaya Tripathi<sup>2</sup>, Ravi Kiran<sup>3</sup>, Manu Santhanam<sup>4</sup>, Gaurav Sant<sup>5</sup>, Narayanan Neithalath<sup>6\*</sup>

## Abstract

3D printed concrete (3DPC) undergoes substantial early-age shrinkage and cracking, driven by its formwork-free nature and high surface area-to-volume ratio that accelerates moisture loss. Measuring early-age deformations in 3DPC is complex because of the local heterogeneity caused by layering variations, overburden effects, print geometry, and the restraint effects that result in non-uniform volume changes. This paper utilizes Digital Image Correlation (DIC) to capture early-age (first 24 h) shrinkage deformations in 3D printed elements made using different binders, and with different layer and filament configurations. DIC-based surface strain measurements accurately capture the rapid volume change due to early drying, and the gradual plateauing as the mixture sets and hardens. The differences in restraint effects—both from the substrate as well as the layers and filaments—impose substantial differences in measured shrinkage. Hence, a novel framework is proposed here to quantify the multi-directional restraint effects, and to decouple them from the measured shrinkage. The result is the extraction of free shrinkage strains (geometry- and restraint independent) in 3DPC that is a function of the mixture design and exposure condition. The framework is validated for multiple layers and filaments with different dimensions as well. The approach, in conjunction with measurements of time-dependent elastic modulus, also allows for the determination of tensile stresses and thus the cracking propensity in in-place 3D printed concrete elements.

**Keywords:** 3D concrete printing (3DCP), shrinkage, digital image correlation (DIC), free shrinkage, and restrain effects.

---

<sup>1</sup> Graduate Student, School of Sustainable Engineering and the Built Environment, Arizona State University, USA

<sup>2</sup> Assistant Research Scientist, School of Sustainable Engineering and the Built Environment, Arizona State University, USA

<sup>3</sup> Associate Professor, School of Sustainable Engineering and the Built Environment, Arizona State University, USA

<sup>4</sup> Professor, Department of Civil Engineering, Indian Institute of Technology Madras, India

<sup>5</sup> Professor, Department of Civil and Environmental Engineering, University of California, Los Angeles, USA

<sup>6</sup> Professor, School of Sustainable Engineering and the Built Environment, Arizona State University, USA \*  
Corresponding author, Email: [Narayanan.Neithalath@asu.edu](mailto:Narayanan.Neithalath@asu.edu)

## 25 1. INTRODUCTION

26 Additive manufacturing (3D printing) of concrete is rapidly gaining attention as a transformative approach  
27 in the construction industry, facilitating the freeform fabrication of structural components through  
28 elimination of traditional formwork [1,2,3,4]. While this layered deposition technology presents  
29 numerous advantages over conventional construction methods, its widespread implementation is still  
30 hindered by several challenges, early-age shrinkage and associated cracking [5,6,7] being an important  
31 one. Immediately after extrusion, the printed elements have their entire surface areas exposed, leading  
32 to increased rate of moisture loss, resulting in significant plastic shrinkage [8,9]. When this shrinkage is  
33 restricted by factors such as overlying layers or non-uniform boundary conditions, tensile stresses  
34 develop, which when exceeds the tensile strength of the concrete, lead to cracking [5,8,10]. 3D-printed  
35 concrete (3DPC) is also more vulnerable to early-age cracking due to the use of higher binder (especially  
36 cement) content, limited bleeding capacity, and absence of coarse aggregates [7,11].

37 Conventional measurement techniques are often inadequate to accurately capture early-age  
38 deformations in 3DPC due to the local heterogeneity introduced by layering variables, overburden effects,  
39 and print geometry [10,12]. Each layer undergoes different mechanical constraints, resulting in  
40 differential drying, and thus varying shrinkage responses across the printed element. The interaction  
41 between substrate and the freshly extruded layers introduces restraint effects, which transmits from the  
42 already printed layer to the successive layers that are printed over it. Furthermore, restraint is introduced  
43 from adjacently placed printed filaments, leading to additional non-uniform volumetric changes.

44 Several studies have focused on quantifying shrinkage in 3DPC [9,10,13,14,15,16,17] and most of them  
45 consider shrinkage to be a bulk response, neglecting the effect of number and thickness of layers,  
46 presence of adjacent filaments, and the evolution of material properties with time and location in the  
47 printed structure. Advanced techniques such as digital image correlation (DIC) and embedded sensors,  
48 such as fiber-optic sensors, have been used to assess shrinkage strains [18,19,20]. Distributed fiber-optic  
49 sensors provide spatially continuous, internally measured early-age strains with appropriate temperature  
50 and moisture compensation, offering a complementary view to surface DIC [21]. DIC- and LVDT-based  
51 techniques have been shown to highlight the significant early-age deformation caused by rapid  
52 evaporation due to increased exposed surface area [7,8,15]. Beyond global deformation mapping, DIC has  
53 also been used to detect and quantify plastic shrinkage cracking in substrate-restrained overlays,  
54 extracting validated crack properties [22]. Studies on plastic shrinkage cracking in 3DPC have shown that  
55 restrained early-age shrinkage leads to rapid crack formation within the first two hours, and promotes  
56 interlayer slip that could compromise bond strength between layers [7]. Parallel capillary-pressure  
57 tracking has further implicated meniscus-driven suction as a governing driver of early-age strain  
58 localization in printed filaments [23]. It has also been shown that increased overburden pressure due to  
59 the superimposed layers enhances bleeding and capillary pressure while simultaneously imposing  
60 restraint-induced tensile stresses at the bottom layers, which increases the risk of early-age cracking [16].  
61 A predictive framework for total shrinkage in 3DPC that couples internal relative humidity, mass loss, and  
62 hydration across specimens with different water-to-cement ratios and surface-to-volume geometries has  
63 been reported [24]. The significance of layer build-up rate on early-age cracking in 3DPC has been  
64 investigated using embedded strain gauges [14], although layer-dependent deformations were not

65 explicitly addressed. While differential shrinkage in 3DPC has been attributed to heterogeneous drying  
66 [7,8] the influence of geometry-induced constraints, such as those arising from layer count (element  
67 height) or filament arrangement, have also not been quantified.

68 Shrinkage-induced deformations in 3DPC result from the combined effect of free shrinkage (driven by  
69 moisture loss) and mechanical restraint arising from the filament laying process, both in the vertical and  
70 horizontal directions. In other words, restraints originate from the confinement imposed by the print bed  
71 in the longitudinal (along the layer build-up direction) and lateral (along the member thickness direction)  
72 directions, both of which limit deformation. A framework capable of resolving shrinkage behavior along  
73 these orthogonal directions is essential for linking moisture-loss kinetics, stiffness development, and the  
74 onset of tensile cracking in 3DPC. This study introduces a methodology that disaggregates observed  
75 deformation into free shrinkage and geometry-induced restraint components, providing a means to  
76 reliably estimate the influence of different mixtures and printing parameters (layer height, overall  
77 thickness, and filament geometry) on shrinkage strains and the potential for early-age cracking. Full-field,  
78 non-contact strain mapping using DIC [7,18,25] is used to isolate directional restraint-induced  
79 deformation across individual printed layers. A simplified mechanics-based approach is used to quantify  
80 restraint in the longitudinal and lateral directions, and experimental results are used to elucidate the  
81 effect of substrate restraint on shrinkage strains. The methodology proposed here allows for the  
82 extraction of shrinkage strains as functions of the material composition and exposure conditions alone,  
83 allowing designers to identify and select binder combinations that minimize shrinkage and associated  
84 cracking concerns in 3DPC.

## 85 **2. EXPERIMENTAL PROGRAM**

### 86 **2.1. Materials**

87 Type I/II ordinary Portland cement (OPC) conforming to ASTM C150, limestone powder conforming ASTM  
88 C568, fly ash conforming to ASTM C618, and a Type IP-equivalent cement conforming to ASTM  
89 C595/C595M, containing 35% (by mass) of calcined clay, were used in this study. The particle size  
90 distributions of OPC, limestone, fly ash, and Type IP cement are illustrated in Figure 1, with their chemical  
91 compositions provided in Table 1. Specific gravities of OPC, limestone, fly ash, and Type IP cement were  
92 determined using a gas pycnometer to be 3.24, 2.80, 2.30, and 2.85 respectively. Three different binder  
93 compositions, consisting of: (i) OPC and limestone (L) (70% and 30% respectively, by mass) denoted as L<sub>30</sub>,  
94 (ii) OPC, limestone (L), and fly ash (F) (70%, 15%, and 15% respectively) denoted as L<sub>15</sub>F<sub>15</sub>, and (iii) Type IP-  
95 equivalent cement (IP), denoted as IP<sub>35</sub> (to indicate that it contains 35% of calcined clay, with a kaolinite  
96 content of 50% by mass in the parent clay) were used, as shown in Table 2. In this study, mixture design  
97 denotes the full formulation, including binder constituents and chemical admixtures (where used). These  
98 mixtures have been previously optimized by the authors [26,27] to satisfy critical requirements for  
99 printability, including favorable particle packing density and rheological behavior. Flow-spread values for  
100 L<sub>30</sub>, L<sub>15</sub>F<sub>15</sub>, and IP<sub>35</sub> were 170-180 mm, determined in accordance with ASTM C1437-15, indicating  
101 comparable fresh workability within the printable window. A commercial medium-grade sand (Quikrete)  
102 conforming to ASTM C778 with a median particle diameter of 0.2 mm and a maximum particle size of 0.6  
103 mm was used as the fine aggregate. The aggregate volume fraction was maintained as 50% of the total  
104 volume of solids across all compositions. A water-to-binder ratio (w/b) of 0.35 was maintained for both

105 cast and printed specimens, to enable sufficient extrudability and buildability. However, a polycarboxylate  
 106 ether-based superplasticizer was required to achieve desired extrudability and buildability for the mixture  
 107 made using Type IP-equivalent cement, owing to the presence of calcined clay. The dry materials were  
 108 premixed for 2 min at a low speed of 136 rpm. The mixing process continued for 3 min at the low speed  
 109 while gradually adding the premixed water-superplasticizer solution. Final homogenization was achieved  
 110 through high-speed mixing at 280 rpm for an additional 2 min.

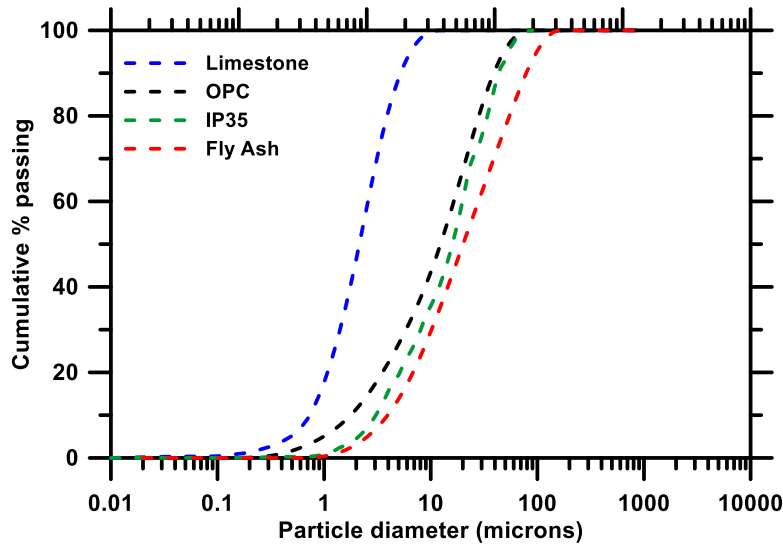


Figure 1: Particle size distribution of the binder systems

111

112

Table 1: Chemical composition of the binder materials

Binder ingredient	Chemical composition (% by mass)								
	CaO (%)	SiO <sub>2</sub> (%)	Al <sub>2</sub> O <sub>3</sub> (%)	Fe <sub>2</sub> O <sub>3</sub> (%)	MgO (%)	SO <sub>3</sub> (%)	Na <sub>2</sub> O (%)	K <sub>2</sub> O (%)	LOI <sup>a</sup> (%)
OPC	63.21	19.60	4.09	3.39	3.37	3.17	0.25	0.16	2.54
Type IP	41.74	36.6	8.84	3.41	1.63	2.82	0.20	0.92	4.42
Fly ash (F)	9.93	54.93	20.44	4.57	2.81	0.86	-	-	0.98
Limestone (L)	CaCO <sub>3</sub> > 99%								

113 <sup>a</sup> Loss on Ignition

114 Table 2: Mortar mixture proportions used in the study. All the mixtures contained medium sand at 50%  
 115 of the volume of solids.

Mixture ID	Mass fraction of binder ingredients				Water-to-binder (w/b) ratio, by mass	Superplasticizer dosage (% by mass of binder)
	OPC	Limestone (L)	Fly ash (F)	Calcined clay (C)		
L <sub>30</sub>	0.70	0.30	0	0	0.35	0
L <sub>15</sub> F <sub>15</sub>	0.70	0.15	0.15	0	0.35	0
IP <sub>35</sub>	0.65	0	0	0.35	0.35	0.50

## 116 **2.2. Measurement of drying shrinkage in cast specimens through extensometer and DIC**

117 Drying shrinkage was evaluated on prismatic mortar specimens (285 mm × 25 mm × 25 mm), in  
118 accordance with ASTM C157 guidelines. The measurement started 24 h after casting, when the samples  
119 were demolded. They were placed in a conditioned environment at  $25 \pm 2$  °C and  $60 \pm 5\%$  relative humidity  
120 (RH). Each test result represents the average of three replicates, and shrinkage data were collected for up  
121 to 28 days.

122 The evolution of strain on the prismatic specimens due to drying shrinkage was also monitored using DIC,  
123 following the same specimen dimensions, conditioning environment, and demolding time as described  
124 above (ASTM C157 procedure). The only modification was the application of black and white acrylic  
125 speckles to the surface prior to testing, after demolding. A DIC setup comprising two synchronized  
126 cameras was positioned to monitor a predefined region of interest on the speckled surface. The cameras  
127 consisted of a stereo pair of Point Grey Grasshopper units (5.0 MP, 2448×2048) with 1/1.8" sensors and  
128 3.45 μm pixel pitch, with an acquisition limit of up to 5 frames per second. Adequate lighting was provided  
129 using high intensity flood lamps, and both cameras were calibrated for optimized aperture and focal clarity  
130 to ensure accurate image acquisition throughout testing. Image frames were recorded at 10 min intervals.  
131 Lagrangian strain fields were derived from displacement maps following standard post-processing  
132 protocols [28,29]. The subsequent analysis used a subset size of 50 pixels and a step size of 12 pixels,  
133 selected to balance spatial resolution and correlation robustness. Results represent the average shrinkage  
134 strain obtained from three specimens, monitored over a period of 28 days.

## 135 **2.3. 3D printing and measurement of early-age shrinkage using DIC technique**

136 Mortar mixtures (L<sub>30</sub>, L<sub>15</sub>F<sub>15</sub>, and IP<sub>35</sub>) were extruded using a gantry-based printing system equipped with  
137 a screw-driven extrusion mechanism. A 30-mm square nozzle was used to print filaments of square cross-  
138 section, 30 mm wide and 30 mm tall. The mixtures enabled prints with smooth surfaces and good inter-  
139 layer and inter-filament bonding. For the initial shrinkage measurements using DIC and quantification of  
140 layer and filament restraint effects on shrinkage, two wall geometries were employed: (i) a single filament  
141 thick wall (400 mm long (*l*) × 30 mm wide (*b*) × 120 mm tall (*d*)), composed of single filament in the  
142 horizontal plane and four layers in vertical plane (Case A; Figure 2(a)), and (ii) a double-filament wall (400  
143 mm long × 60 mm wide × 120 mm tall), composed of two filaments in the horizontal plane and four layers  
144 in vertical plane (Case B; Figure 2(b)). In these figures, the x–y plane represents the print bed, with the x-  
145 direction along the print length and the y-direction along the filament width (thickness), while the z-  
146 direction corresponds to the layer build-up direction. Case A considers restraint only in the vertical (z-  
147 direction), while Case B assesses the influence of lateral (y-direction) restraint as well.

148 To validate the restraint effects under varying layer, filament numbers and sizes, three additional walls  
149 were printed using the L<sub>30</sub> mixture: (i) a single-filament wall, similar to Case A but of shorter height (400  
150 mm long × 30 mm wide × 90 mm tall; Figure 2(c)) having only three layers, (ii) a four-filament wall (400  
151 mm long × 120 mm wide × 120 mm tall; Figure 2(d)) of identical height and length to Cases A and B, but  
152 double the width, and (iii) a six-filament wall (400 mm long × 120 mm wide × 120 mm tall; Figure 2(e))  
153 with same overall size as the previous case, but printed using a 20-mm square nozzle, so as to have more  
154 filaments and layers. These additional configurations were designed to validate layer build-up and

155 filament-dependent restraint behavior, including the effect of differing filament widths. The first layer in  
 156 all configurations corresponds to the filament placed directly on the print bed, followed sequentially by  
 157 the upper layers. For the prints with multiple filaments, all filaments in the first layer were printed first  
 158 before overlaying the layers.

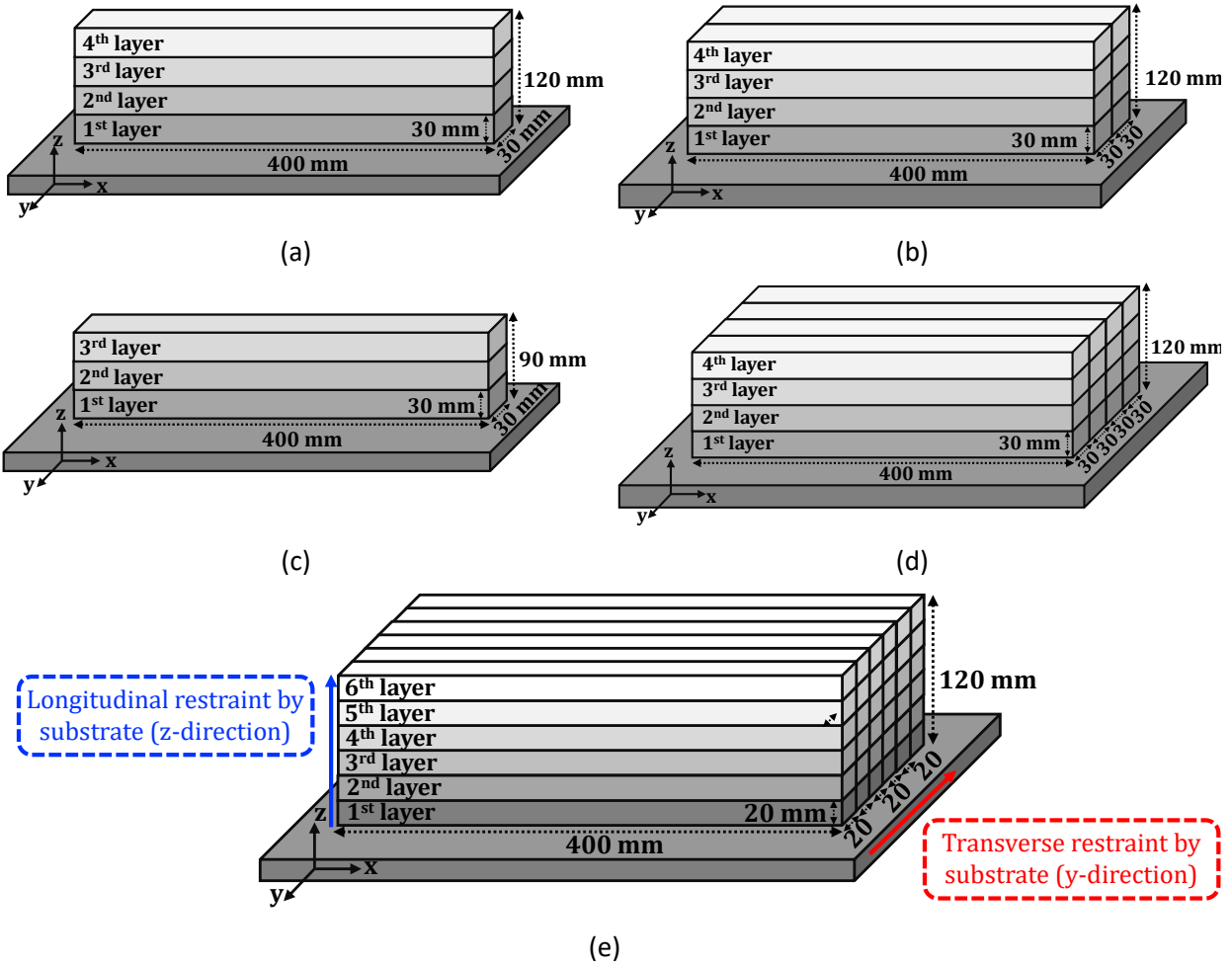


Figure 2: Geometries of 3D printed wall specimens used for early-age shrinkage evaluation: (a) single-filament wall (400 × 30 × 120 mm), (b) double-filament wall (400 × 60 × 120 mm), (c) single-filament wall of reduced height (400 × 30 × 90 mm), (d) four-filament thick wall (400 × 120 × 120 mm), and (e) six-filament thick wall with 20-mm square filaments (400 × 120 × 120 mm).

159

160 An in-plane print speed of 30 mm/s and a vertical speed of 5 mm/s was used, with the auger speed  
 161 calibrated to obtain a consistent extrusion rate of 27 ml/s. Immediately after printing (Figure 3(a)), the  
 162 exposed surface of the fresh concrete was speckled with white acrylic paint, with the greyish color of the  
 163 printed mixture serving as the background (Figure 3(b)). Image acquisition commenced soon after and  
 164 continued for the first two hours to track the very early-age deformation. After this initial phase, image  
 165 acquisition was suspended for approximately 15 min to allow application of a dual speckle pattern—a  
 166 white acrylic paint serving as the background and speckles created using black acrylic paint (as shown in

167 Figure 3(c)). Measurements were resumed and continued for an additional 22 h. In this work, early-age  
 168 deformation denotes the total strain evolution from printing up to 24 h. This protocol enabled capturing  
 169 of the time-dependent early-age shrinkage behavior for the initial 24 h, with minimum loss of data (~ 15  
 170 min which was required for drying of the white paint at the start of second phase). The DIC-based strain  
 171 map in Figure 3(d) includes virtual extensometers (E0 to E3) placed at the mid-height of each printed layer,  
 172 enabling quantification of deformation at different heights. The experimental set up adopted for DIC-  
 173 based monitoring is schematically illustrated in Figure 4, which ensures accurate capture of full-field  
 174 early-age deformations throughout the measurement period. The DIC measurements reflect the total  
 175 shrinkage under the prevailing restraint conditions. Unless otherwise noted, all specimens were printed  
 176 on a plexiglass base to ensure a consistent surface condition.

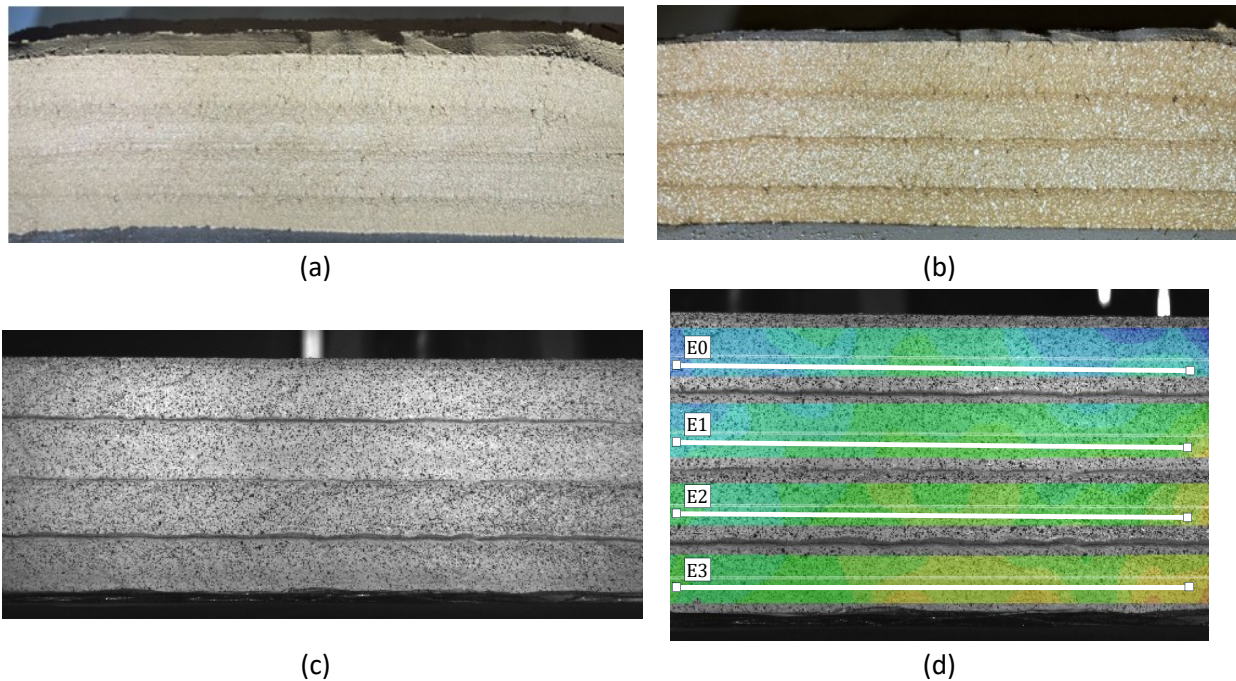


Figure 3: DIC-based setup for early-age shrinkage monitoring in 3D printed walls: (a) freshly printed four-layer wall; (b) white speckle pattern applied on fresh surface; (c) dual-speckle pattern with layer labels (1<sup>st</sup> layer nearest to print bed); (d) DIC strain map with virtual extensometers (E0-E3) placed at mid-height of each layer for deformation analysis.

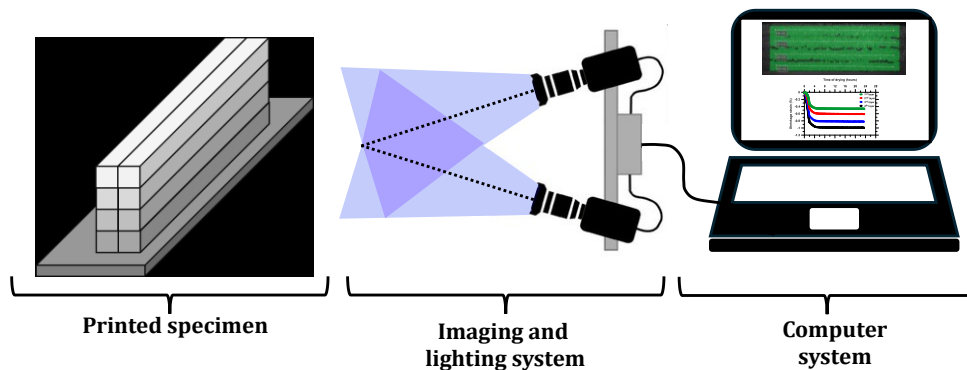


Figure 4: Schematic configuration of the imaging setup utilized for DIC

177 **2.4. Exposure conditions for severe drying of printed specimens**

178 In addition to the prints described above, single-filament wall elements with four layers (400 mm long ×  
179 30 mm wide × 120 mm tall) were printed and subjected to a controlled severe-drying environment in an  
180 attempt to induce early-age plastic shrinkage cracking. Immediately after printing, the specimens were  
181 placed under a directed air flow of approximately 3 m/s at  $25 \pm 2$  °C and  $60 \pm 5$  % RH to promote rapid  
182 surface evaporation. DIC measurements were initiated concurrently to capture the time-dependent  
183 deformation and the onset of surface cracking.

184 **2.5. Reduction of substrate restraint through low-friction interface**

185 To investigate the effect of substrate-induced restraint on early-age shrinkage, a separate set of  
186 single-filament, four-layer wall specimens (400 mm long × 30 mm wide × 120 mm tall) was printed over a  
187 low-friction interface. Friction effects were minimized by sequentially placing a plastic sheet, applying a  
188 thin layer of oil, and covering it with an additional plastic layer before printing. This arrangement  
189 minimized interfacial shear transfer from the substrate to the base filament, thereby lowering z-direction  
190 restraint at the print bed. Digital image correlation (DIC) measurements were performed under the same  
191 severe-drying exposure as mentioned above to monitor the early-age deformation under the reduced  
192 restraint condition.

193 **2.6. Measurement of stiffness evolution at early times**

194 To quantify the time-dependent evolution of stiffness in printed mortar mixtures, Green Compression  
195 Tests (GCT) were performed on fresh extruded specimens at predetermined intervals using appropriate  
196 modifications to a protocol developed and reported earlier [30]. Mortar was extruded through a 30 mm  
197 square nozzle to fabricate a rectangular cuboid (600 × 90 × 120 mm). Immediately after printing, six  
198 cylinders (50 mm diameter × 100 mm height) were carefully extracted from the cuboid. The stainless-steel  
199 coring tube was internally lubricated to minimize friction and avoid geometric distortion during extraction.  
200 After coring, excess material was trimmed and the specimen was carefully ejected and leveled to ensure  
201 flat, parallel loading surfaces. The cylindrical surfaces were then coated with a dual-speckle pattern (white  
202 background with black speckles) using acrylic paint, to facilitate DIC-based strain measurement. The  
203 cylinders were then subjected to the severe drying exposure condition described earlier, to ensure that  
204 the modulus values would be representative of those relevant to the desired exposure conditions. The  
205 specimens were tested after 30, 60, 90, 120, 150, and 180 min from printing.

206 GCT was performed using a displacement-controlled universal testing machine (MTS Exceed Series 40 E42,  
207 5 N-5 kN capacity). Acrylic platens were used at both ends to achieve uniform and aligned contact. A small  
208 pre-conditioning displacement (< 0.5 mm) was applied to ensure proper seating. A quasi-static loading  
209 rate of 1 mm/min (strain rate of 0.01/min) was used. DIC was used to capture full-field strain distributions  
210 and detect strain localizations or heterogeneity during testing. The stress-strain response was derived  
211 using machine-recorded load data and DIC-based deformation measurements. The modulus of elasticity  
212 at each time interval was computed by applying linear regression to the initial (elastic) portion of the  
213 stress-strain curve, prior to the onset of yielding. This procedure enabled reliable and repeatable  
214 assessment of the early-age stiffness of the printed mortars under relevant drying and loading conditions,  
215 allowing for accurate determination of restraint-induced stress development.

216 **3. RESULTS AND DISCUSSIONS**

217 **3.1. Ascertaining DIC as an appropriate method for shrinkage measurements**

218 Figure 5 presents a comparison of the total shrinkage strain over a period of 28 d, obtained from the  
219 traditional extensometer-based measurements (ASTM C 157) and the DIC-based measurements for the  
220 same binder prisms. The results indicate a strong correlation between both measurement techniques,  
221 confirming that DIC captures shrinkage behavior that is consistent with the extensometer readings.  
222 Furthermore, the application of an acrylic black-and-white speckle pattern on the specimen did not  
223 adversely affect the measured shrinkage response, thus demonstrating the reliability of DIC for capturing  
224 deformation behavior in cementitious materials.

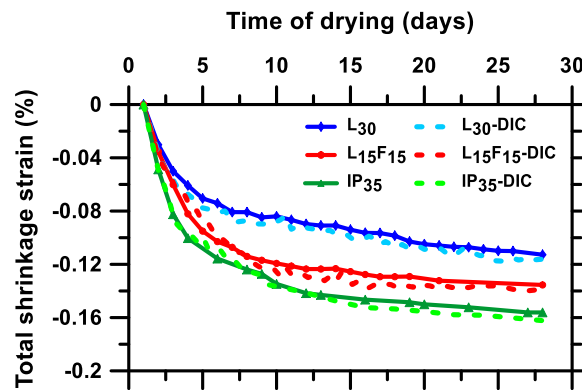


Figure 5: Comparison of total shrinkage strain over time measured based on ASTM C 157 procedure and DIC for different binder systems. The measurements started after demolding, which occurred 24 h after casting. The average strains shown here represent three replicate samples, with uncertainties < 5% of the average.

225 **3.2. Layer and filament restraint effects on shrinkage behavior in 3D printed concrete**

226 Figure 6 and Figure 7 illustrate the DIC-based shrinkage strain profiles at various heights for the three  
227 different binder systems (L<sub>30</sub>, L<sub>15</sub>F<sub>15</sub>, and IP<sub>35</sub>), for the single-filament (Case A) and double-filament (Case  
228 B) prints respectively, corresponding to schematics in Figure 2(a) and (b). The DIC strain measurements  
229 correspond to the mid-height of each printed layer. The 1<sup>st</sup> layer is the bottom-most layer in contact with  
230 the print base, and the 4<sup>th</sup> layer is the top-most. Note that the DIC-measured strains shown in Figure 6  
231 and Figure 7 correspond to the time period before the measurements started in the experiments reported  
232 in Figure 5. Initial setting times for all mixtures fell within a narrow range (70-80 min), minimizing setting-  
233 related bias in moisture loss and shrinkage interpretation. All the three binder systems exhibit similar  
234 shrinkage profiles ( $\epsilon_{observed}$ ), with significant strain development during the first ~ 4 h (primary regime),  
235 followed by gradual plateauing (secondary regime). This behavior is primarily attributed to the accelerated  
236 evaporation of free water from the freshly extruded surface, which leads to volumetric contraction. As  
237 hydration progresses, the setting and hardening process initiates a reduction in evaporation rate, thereby  
238 stabilizing the strain profile. Similar observations of early shrinkage profile governed by surface  
239 evaporation and setting have been reported elsewhere [7,17].

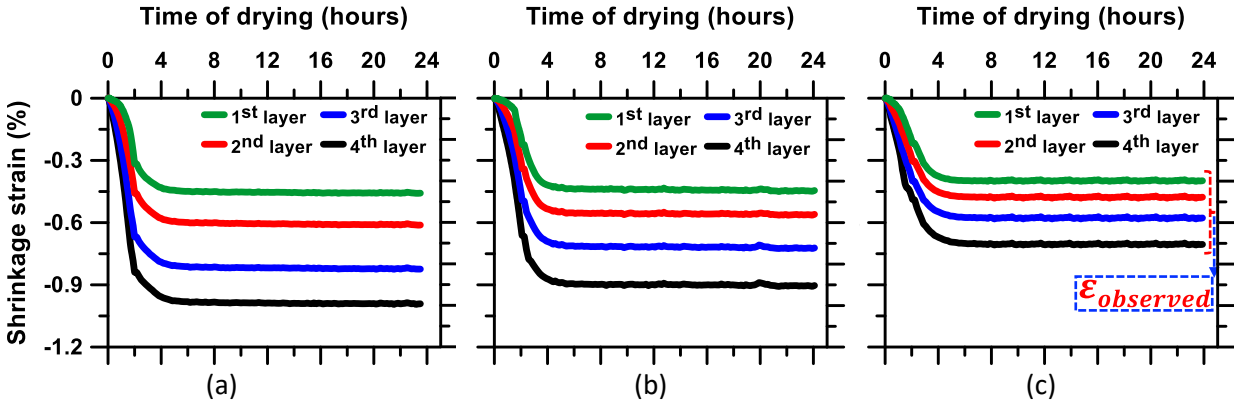


Figure 6: Shrinkage strain profiles at various layer heights for single filament prints, for different binder systems: (a)  $L_{30}$ , (b)  $L_{15}F_{15}$ , and (c)  $IP_{35}$ . Replicate measurements within 5% of each other.

240

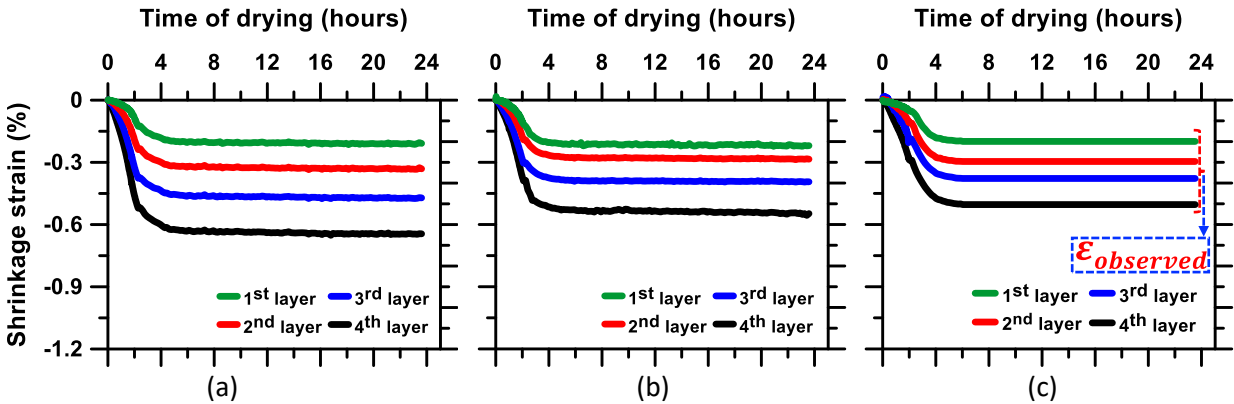


Figure 7: Shrinkage strain profiles at various layer heights for double filament prints, for different binder systems: (a)  $L_{30}$ , (b)  $L_{15}F_{15}$ , and (c)  $IP_{35}$ . Measurements are based of three replicate prints, with variability < 8%.

241

242 For all the mixtures and in both configurations, the top-most layer experiences the highest shrinkage  
 243 strain and bottom-most layer, the lowest, attributable to restraint effects. Restraint refers to the  
 244 displacement restrictions imposed on the printed element due to boundary conditions, which in turn  
 245 result in the restriction of the free volumetric contraction of concrete. For the single-filament prints, the  
 246 shrinkage strain after 24 h is  $\sim 0.42\%$  at the 1<sup>st</sup> layer for the  $L_{30}$  mixture, increasing to  $\sim 1.0\%$  at the 4<sup>th</sup> layer.  
 247 As expected, for the double-filament prints where the restraint in the lateral direction is also active, the  
 248 strains are further lower – for the  $L_{30}$  mixture, it varies from  $\sim 0.21\%$  at the 1st layer to  $\sim 0.65\%$  at the 4th  
 249 layer. Furthermore, the shrinkage strains in the double-filament prints are noted to exhibit less variation  
 250 across layers, once again attributed to the enhanced restraint that restricts movement. The shrinkage  
 251 strains are found to be lower for the  $L_{15}F_{15}$  and the  $IP_{35}$  mixtures as compared to the  $L_{30}$  mixture. The lower  
 252 shrinkage strains in the  $IP_{35}$  mortar as compared to the limestone-containing mortars until 24 h can be  
 253 attributed to higher water retention by the calcined clay, and its slower hydration reactions [31,32]. The  
 254 higher limestone filler content in the  $L_{30}$  mixture increases fines and surface area, suppresses bleeding,  
 255 and promotes surface moisture loss, resulting in higher shrinkage [33,34]. After 24-48 h, this trend  
 256 reverses (see Figure 5), where the fine limestone particles ( $d_{50} \approx 2 \mu\text{m}$ ) contribute to nucleation effects

257 and enhanced pore refinement, while the effects of the other supplementary cementing materials are  
258 slow to manifest [35,36].

### 259 **3.3. Quantification of multidirectional restraint effects**

260 The measured shrinkage strains are influenced not only by material properties but also by geometric  
261 confinement in both longitudinal and lateral directions. The print bed restricts deformation at the base,  
262 resulting in the highest degree of restraint near the bottom of the printed element, as noticed in the  
263 shrinkage strains in Figure 6 and Figure 7. The less stiff (than the print base) layers restrict the movement  
264 of the overburden layers resulting in shrinkage in subsequent layers that is higher than that in the layer  
265 below. Previous studies have acknowledged the contribution of overburden effects, layer-wise  
266 deposition, and inter-filament interactions to anisotropic stress development and early-age cracking in  
267 3DPC systems [37,38]. However, such effects have not been quantified to provide accurate descriptors of  
268 the effect of directional restraint on volume change phenomena. This section introduces a simplified  
269 framework to correct for geometry-induced restraints in both vertical and lateral directions in 3DPC, in an  
270 effort to extract the material's true shrinkage response and elucidate the effects of layer and filament  
271 characteristics on shrinkage. While previous experimental approaches [7,9,10,19,37] provide insights into  
272 early-age strain evolution, they typically measure total deformation without separating layer-wise  
273 deformations or isolating the contribution of the geometry-induced restraints.

274 Figure 8 illustrates the stepwise framework for evaluating early-age deformation in 3DPC, with the goal  
275 of separating the restraint effects in both lateral and vertical directions (due to layers and filaments) from  
276 the DIC-based shrinkage response. To demonstrate the robustness of the analytical model proposed to  
277 extract the free shrinkage separated from the effects of restraints, a DIC-based normalization procedure  
278 was used and implemented on three distinct mixture designs ( $L_{30}$ ,  $L_{15}F_{15}$ ,  $IP_{35}$ ) under fixed  $w/b = 0.35$ ,  
279 constant sand volume fraction, identical geometries, and identical exposure. The model is structured in  
280 three stages. In the first stage, total shrinkage strain is determined based on DIC measurements, with  
281 measurements taken near the mid-height of each printed layer during the initial 24 h after printing. Note  
282 that the deformation can be quantified at any location along the print height, and the analysis yields  
283 comparable results. In the second stage, the observed strains are adjusted to account for the restraint  
284 effects due to the print bed (and underlying layers) on the layers in the build-up direction (in the z-  
285 direction). In the third stage, the adjusted strains from the second stage are further corrected to account  
286 for the restraint induced by additional filaments in the y-direction. With these corrections (two-stage  
287 normalization), the geometry-induced constraints are separated, and the result is the free shrinkage  
288 response of the printed material, which is a function of continuing chemical reactions and exposure  
289 conditions.

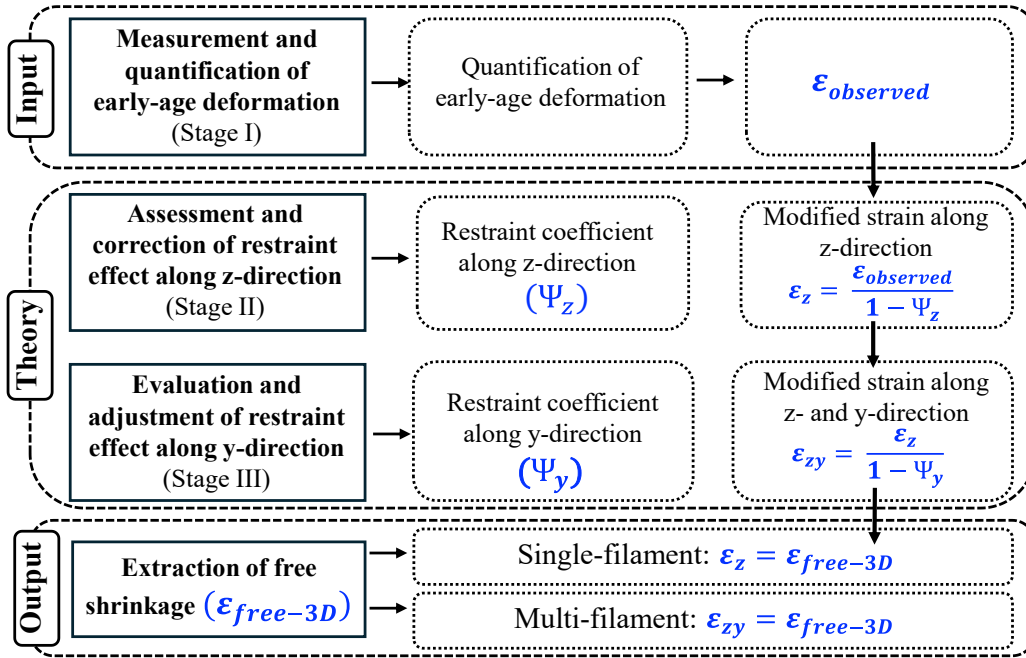


Figure 8: Flow diagram showing the steps involved in evaluating restraint effects to determine free shrinkage.

290

### 291 3.3.1. Measurement and quantification of early-age deformation

292 This step involves measuring the observed deformation ( $\epsilon_{observed}$ ; see Figure 6 and Figure 7) at the mid-  
 293 height of each printed layer using DIC during the first 24 h after printing. In lieu of average deformation  
 294 that is generally recorded, the DIC-based measurement captures layer-wise deformation, thereby  
 295 enabling a more localized and accurate analysis that accounts for the heterogeneity introduced during the  
 296 printing process. This approach also allows to predict cracking time and location also, based on observed  
 297 strain concentrations.

### 298 3.3.2. Accounting for longitudinal restraint effects in the layer build-up direction (z-direction)

299 In 3DPC components, the base layers experience significant restraint due to the stiffness of the substrate  
 300 which restricts free shrinkage, resulting in lower observed deformations [8,14]. In this study, longitudinal  
 301 (z-direction) restraint is treated primarily as a substrate-induced one that transmits upward through the  
 302 height of the wall, producing a restraint field that is maximum at the base and decays toward the top. The  
 303 top-most layer can be considered to experience a near-zero restraint. Although this vertical gradient in  
 304 restraint has been acknowledged [7,10,16], the influence of such differential restraint on early-age  
 305 deformation behavior has seldom been quantified. Hence, a restraint coefficient in the z-direction ( $\psi_z$ ) is  
 306 introduced here.  $\psi_z$  is defined as the ratio of vertical deformation at a given layer height ( $\delta_z$ ) to the total  
 307 vertical deformation of the entire printed wall ( $\delta_{total}$ ) as shown in Equation 2.1 which quantifies the  
 308 degree of restraint experienced at each layer height.

$$\psi_z = \frac{\text{Deformation}_z}{\text{Total deformation}} = \frac{\delta_z}{\delta_{total}} \quad (\text{Equation 2.1})$$

309 Since the printed concrete is assessed during the fresh state, deformation comprises both elastic and  
 310 plastic components due to the material's thixotropic and partially set nature:

$$\delta = \delta_{elastic} + \delta_{plastic} \quad (\text{Equation 2.2})$$

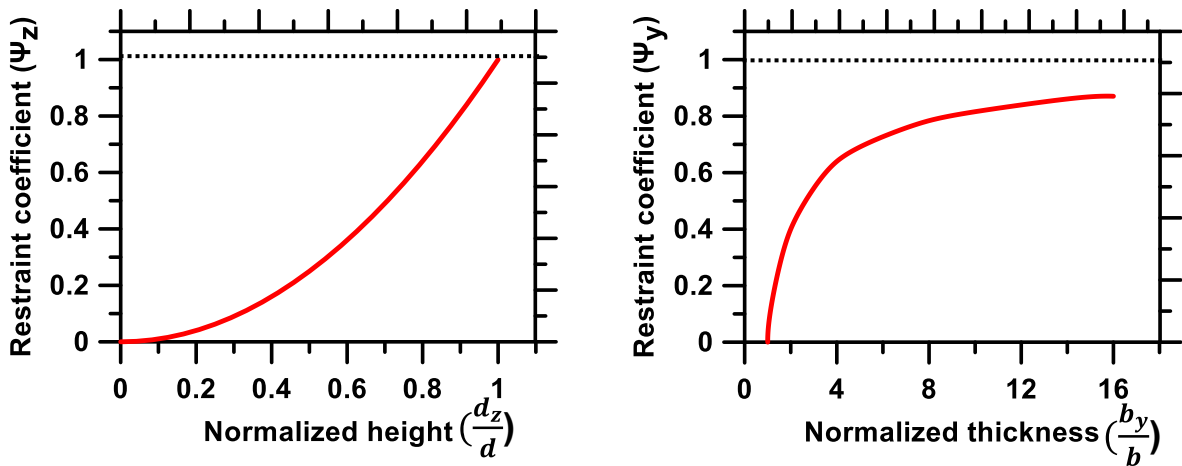
311

312 However, green compression tests on samples extruded from the printed specimens indicated that the  
 313 maximum self-weight-induced stress at the bottom filament at different times remained below the  
 314 corresponding elastic yield stress of the mortar. Consequently, the observed vertical deformation can be  
 315 considered to be primarily elastic ( $\delta_{elastic}$ ), given by Hooke's law. The effective load acting at height  $d_z$  is  
 316 influenced by the weight and build-up of material above, where  $d_z$  is the vertical distance from the top of  
 317 the print to the layer of interest. Thus, the axial load ( $P_z$ ) acting at different distances from the top can be  
 318 expressed in terms of the material unit weight ( $\rho$ ) and geometry, as  $P_z = \rho A d_z$ . Given that the cross-  
 319 sectional area of interest for the self-weight ( $A = l \times b$ ) and the elastic modulus ( $E$ ) remains the same, the  
 320 longitudinal restraint coefficient  $\psi_z$  can be expressed as:

$$\psi_z = \frac{\delta_z}{\delta_{total}} = \left(\frac{d_z}{d}\right)^2 \quad (\text{Equation 2.3})$$

321

322 This formulation indicates that  $\psi_z$  varies quadratically with normalized height, increasing from zero at the  
 323 top (where  $d_z = 0$ ) to unity at the base (where  $d_z = d$ ). By definition,  $\psi_z$  is always bound between 0 and  
 324 1 ( $0 < \psi_z < 1$ ). This boundary condition is physically governed by the progressively increasing  
 325 confinement from accumulated self-weight and substrate interaction. To express the restraint variation  
 326 in a generalized form, it is expressed here as a function of a non-dimensional parameter ( $d_z/d$ ), which  
 327 varies from 0 at the top to 1 at the bottom. As illustrated in Figure 9(a), the bottom-most layer,  
 328 constrained by both substrate interaction and accumulated overburden, experiences maximum restraint,  
 329 while the top-most layer, being minimally confined, exhibits near-zero restraint.



(a)

(b)

Figure 9: Restraint effects in 3DPC elements: (a) as a function of height (z-direction) and (b) as a function of thickness (y-direction). In (b), values are normalized to the minimum section thickness, with a single 30 mm filament case taken as the one with zero lateral restraint.

330

331 Normalizing the observed deformation with  $(1-\psi_z)$ , as shown in Equation 2.4, yields the intrinsic  
 332 shrinkage strain ( $\varepsilon_z$ ), effectively eliminating the influence of longitudinal restraint along build-up  
 333 direction. Note that, if there is only one filament being built up, this is effectively the free shrinkage strain,  
 334 ( $\varepsilon_z = \varepsilon_{free-3D}$ ), which is a function of the mixture characteristics and the exposure conditions.

$$\varepsilon_z = \frac{\varepsilon_{observed}}{1 - \psi_z} \quad (\text{Equation 2.4})$$

### 335 3.3.3. Accounting for lateral restraint along thickness (y-direction)

336 The third stage of the model addresses the restraint effects induced by the thickness (y-direction) of the  
 337 printed element, particularly those associated with increasing wall thickness or filament count. Previous  
 338 studies have recognized that thicker printed elements tend to exhibit reduced deformation due to  
 339 enhanced lateral confinement [10,39]. Figures 6 and 7 clearly show that, for all the mixtures tested, even  
 340 at the top-most layer where longitudinal (z-direction) restraint is minimal, double-filament walls exhibit  
 341 approximately 35% lower strain compared to single-filament walls, indicative of the presence of lateral  
 342 (transverse) restraint in multi-filament walls. Here, a restraint coefficient in the y-direction ( $\psi_y$ ), is  
 343 introduced, that complements  $\psi_z$  defined earlier for the z-direction.

344 Since  $\psi_y$  is the restraint factor in the lateral direction, it can be considered to be zero for a single-filament  
 345 print (unless a single filament wall is printed to thicken an existing wall, as in the case of structural  
 346 strengthening or for architectural purposes—such cases are not considered here). Thus, the relationship  
 347 between the shrinkage strains in the z-direction for a single and double filament print can be expressed  
 348 as:

$$\varepsilon_z^{(single)} = \frac{\varepsilon_z^{(double)}}{1 - \psi_y} \quad (\text{Equation 2.5})$$

349 For each binder system used here,  $\psi_y$  was determined by equating the free shrinkage strain of a single-  
 350 filament wall to that of a double-filament wall after removing the z-direction restraint as described above.  
 351 To accomplish this, experimental results from one-, two-, and four-filament walls were used,  
 352 corresponding to wall thicknesses of 30, 60, and 120 mm respectively. These correspond to normalized  
 353 thicknesses of 1, 2, and 4 in Figure 9(b). The first few points in Figure 9(b) are thus derived from  
 354 experimental results and averaged over multiple trials (with standard deviations found to be less than  
 355 1.5%), and similar values were obtained across different binder systems. Beyond a normalized thickness  
 356 value of 4,  $\psi_y$  was extended by scaling the experimentally determined ratio of reduction in free shrinkage  
 357 with each doubling of thickness, which was determined to 0.65, irrespective of the material type. In other  
 358 words,  $\varepsilon_{free-2t} = 0.65 \varepsilon_{free-t}$ ;  $\varepsilon_{free-4t} = 0.65 \varepsilon_{free-2t}$  (where  $\varepsilon_{free-t}$ ,  $\varepsilon_{free-2t}$ , and  $\varepsilon_{free-4t}$  are free  
 359 shrinkages at wall thicknesses of t, 2t, and 4t respectively). It is seen (based on limited experiments shown  
 360 in a later section of this paper) that this ratio remains effectively invariant across reasonable changes in

361 layer width and height when the overall thickness is matched. The subsequent points were therefore  
362 extrapolated to illustrate the asymptotic approach of  $\psi_y$  towards unity with increasing thickness (e.g.,  
363 increasing number of filaments).

364 This approach ensures that  $\psi_y$  captures the additional restraint introduced by increasing thickness. As the  
365 number of filaments increases, the lateral restraint becomes more pronounced, and  $\psi_y$  increases, slowly  
366 approaching unity in significantly thicker cross-sections (as illustrated in Figure 9(b)). Figure 9(b) also  
367 shows the diminishing marginal enhancement in restraint as thickness is increased. In other words, this  
368 parameter theoretically remains lower than 1.0 even in very thick sections (even at a  $b_y/b$  of 16, it is only  
369  $\sim 0.90$ ). This coefficient represents the fraction of deformation prevented by lateral confinement relative  
370 to an unconstrained single-filament and is also theoretically bounded between 0 and 1 ( $0 < \psi_y < 1$ ). A  
371 value of zero indicates no lateral restraint, while a value of 1.0 represents a fully restrained cross-section.

372 The previously height-adjusted strains ( $\varepsilon_z$ ) are further normalized using  $(1 - \psi_y)$ , yielding  $\varepsilon_{zy}$  (Equation  
373 2.6), which represents the case where the experimental shrinkage of a 3D printed wall is adjusted for both  
374 the z- and y-direction geometric effects, yielding the intrinsic free strain that is representative of the  
375 material and exposure effects.

$$\varepsilon_{zy} = \frac{\varepsilon_z}{1 - \psi_y} \quad (\text{Equation 2.6})$$

376

377 The validity and generality of the experimentally derived  $\psi_y$  values are further assessed using multi-  
378 filament ( $\geq 4$ ) configurations, as discussed in the following sections.

### 379 **3.4. Implementation of the multidirectional restraint factors on DIC-based strain measurements**

#### 380 *3.4.1. Correction for longitudinal restraint effects in the layer build-up (z-direction)*

381 Figure (a) and (b) illustrate the shrinkage strain normalized by the z-direction restraint coefficient (as  
382 described in Equation 2.4) for both single- and double-filament prints for the  $L_{30}$  mixture. The observed  
383 strains were shown in Figures 6(a) and 7(a) respectively. The layer height  $d_z$  corresponding to each virtual  
384 extensometer (E0 to E3), as captured in the DIC-based strain maps (see Figure 3(d)), was used to compute  
385 the restraint coefficient  $\psi_z$  at each layer using Equation 2.3.

386 Upon applying the z-direction correction, the observed strain  $\varepsilon_{observed}$  for different layers converge,  
387 indicating that the previously observed variation in shrinkage between layers can primarily be attributed  
388 to the restraint imposed by the substrate and to a lesser degree, the underlying layers (since the extrusion  
389 time interval between layers is minimal, the restraint imposed by the underlying layers can be considered  
390 to be minor. If the overlying layer is laid after one immediately below has set, this will still be captured in  
391  $\psi_z$ ). The z-direction normalized strain values obtained from this step are referred to as  $\varepsilon_z$  (as shown in  
392 Figure (a) and (b)). In the case of single-filament specimens (Figure (a)), the  $\varepsilon_z$  values represent the  
393 intrinsic free shrinkage strain  $\varepsilon_{free-3D}$ , assuming the lateral restraint to be negligible in such slender  
394 geometries. This assumption allows  $\varepsilon_z$  to serve as the baseline for evaluating additional restraint effects

395 in multi-filament configurations. For single filament prints, Figure (a) shows that the normalized shrinkage  
 396 strain ( $\epsilon_z = \epsilon_{free-3D}$ ) for the L<sub>30</sub> mixture is about 1.0%. This is equal to the strain in the top-most layer  
 397 observed from the DIC experiments for this mixture, which is expected because the calculation scheme  
 398 for restraint assumes a  $\psi_z$  of zero for the top-most layer. Similar trends were observed for L<sub>15</sub>F<sub>15</sub> and IP<sub>35</sub>  
 399 mixtures; their plots are not shown here since no additional insights are gleaned beyond the differences  
 400 in peak magnitude (~0.9% and ~0.7%, respectively). For double filament walls, Figure (b) similarly shows  
 401 the results for the L<sub>30</sub> mixture, with the shrinkage adjusted for z-direction restraint ( $\epsilon_z$ ). The peak  
 402 shrinkage value for the L<sub>30</sub> mixture was ~0.65%, whereas for the L<sub>15</sub>F<sub>15</sub> and IP<sub>35</sub> mixtures (not shown here),  
 403 the values were ~0.58% and ~0.55%, respectively.

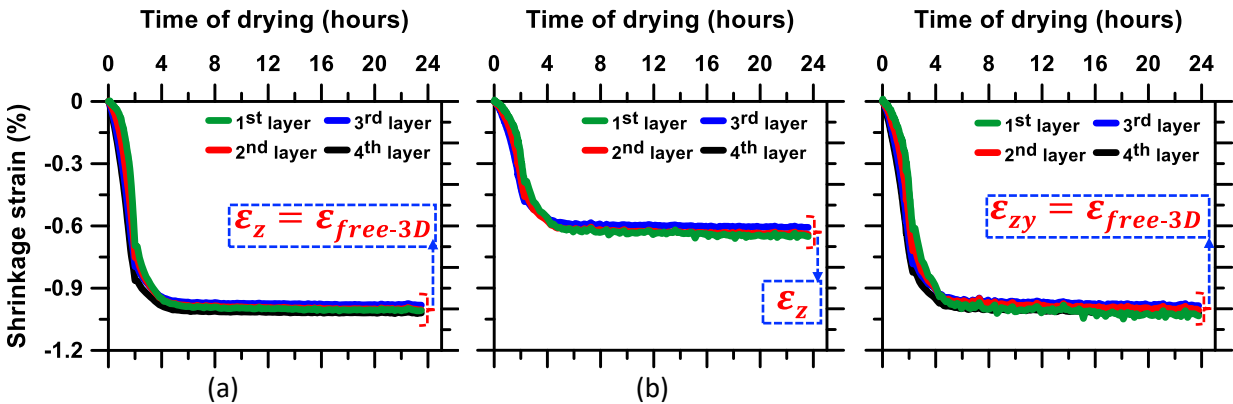


Figure 10: Normalized shrinkage strain for L<sub>30</sub> mixture in: (a) a single-filament wall corrected for longitudinal (z-direction) restraint, (b) a double-filament wall corrected for longitudinal (z-direction) restraint, and (c) a double-filament wall after correction for longitudinal (z-direction) and lateral (y-direction) restraints

404

405 When Figures 10(a) and (b) are compared, it can be seen that, even after applying the z-direction-based  
 406 correction, the double-filament prints (shown in Figure (b)) continue to show reduced strains than the  
 407 single-filament prints, suggesting the role of lateral or transverse restraint in thicker sections. Such lateral  
 408 effects can be attributed to interfacial bonding between adjacent filaments, which restricts movement  
 409 perpendicular to the print direction. Thus, while accounting for substrate and layer restraint alone is  
 410 sufficient in slender geometries, wider or multi-filament elements require consideration of lateral  
 411 restraint effects also, as shown below.

### 412 3.4.2. Correction for lateral restraint along thickness (y-direction)

413 Studies have shown that lateral confinement becomes increasingly significant with increasing element  
 414 width [9,40]. These effects are particularly pronounced during the initial setting period, when the material  
 415 retains sufficient plasticity to undergo volumetric changes but begins to experience restraint from  
 416 adjacent filaments.

417 Figure (c) presents the shrinkage strain profiles for the double-filament L<sub>30</sub> mixture prints after accounting  
 418 for the lateral (y-direction) restraint effects on shrinkage strains on which longitudinal restraint  
 419 corrections have already been implemented. The resulting strain ( $\epsilon_{zy}$ ), corrected for both vertical (build-  
 420 up direction) and lateral (additional thickness) geometric effects, is the free shrinkage strain ( $\epsilon_{free-3D}$ ),

421 as it reflects the material's deformation response independent of external restraint. It can be seen that  
 422 the strain profiles of all the layers converge, and exhibit strong similarity with the trends and values  
 423 observed after longitudinal correction alone in the single-filament specimens (Figure (a)). This similarity  
 424 confirms that once both z- and y-direction geometric effects are systematically corrected, the underlying  
 425 shrinkage behavior is independent of filament configuration. For the double-filament configuration,  
 426 Figure (c) presents the normalized shrinkage strain ( $\epsilon_{zy} = \epsilon_{free-3D}$ ) for the L<sub>30</sub> mixture, which reached a  
 427 peak of approximately 1.0%. The corresponding peak strains for L<sub>15</sub>F<sub>15</sub> and IP<sub>35</sub> mixtures, which also  
 428 followed the same trends as shown in the figures, were around 0.9% and 0.7%, respectively. Thus, the  
 429 approach proposed here not only enables direct comparison of shrinkage strain across different print  
 430 geometries but also provides a consistent framework to evaluate the material's deformation capacity free  
 431 from boundary-induced artifacts.

### 432 3.5. Validation of the multidirectional restraint correction approach

433 All the validation exercises presented in this section utilize the L<sub>30</sub> mixture. Figure 11 illustrates the  
 434 validation of the proposed z-direction-based restraint correction using a single-filament (30 mm wide),  
 435 three-layer (30 mm tall layers) wall element. The DIC-based early-age shrinkage strains ( $\epsilon_{observed}$ ) are  
 436 shown in Figure 11(a). The strain profiles after decoupling the influence of z-direction restraint (using  
 437 Equation 2.4) are shown in Figure 11(b). Since there is only one filament in this case,  $\epsilon_z$  is the same as  
 438  $\epsilon_{free-3D}$ . The strain profiles and ultimate strain values for the L<sub>30</sub> mixture (~ 1.0%) evaluated here are the  
 439 same as those from earlier experiments involving four-layer single- and double-filament prints of the same  
 440 binder.

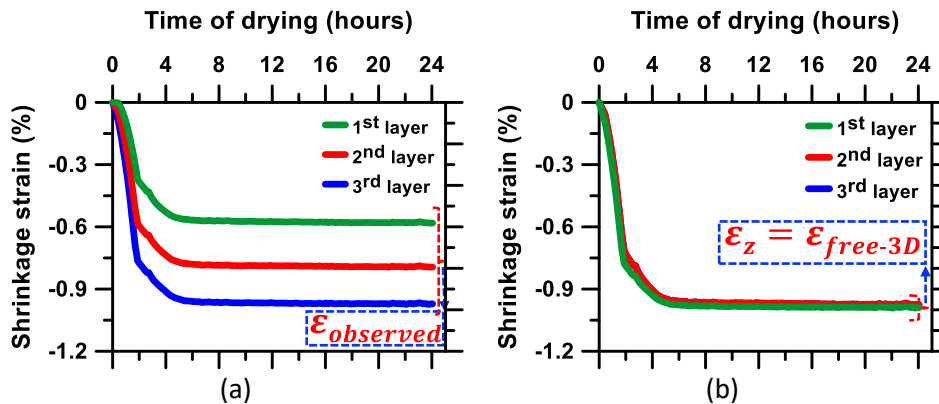


Figure 11: Shrinkage strain profiles for a single filament print wall made using L<sub>30</sub> mixture: (a) at various layer heights, and (b) after z-direction restraint correction. Data are based on three replicates; measurements within 5% of each other.

441  
 442 DIC-measured strain profiles ( $\epsilon_{observed}$ ) for a four-filament (30 mm wide each), four-layer (30 mm tall  
 443 layers) wall element printed using the L<sub>30</sub> mixture are shown in Figure 12(a). Note that the overall strains  
 444 in the layers are much lower than those in the single- or double-filament walls shown in Figures 6(a) and  
 445 7(a) respectively. After implementing the correction for the longitudinal restraint, the resultant strains  
 446 are shown in Figure 12(b). Note that, with increasing number of filaments, the measured maximum strain

447 is significantly reduced ( $\sim 0.6\%$  in Figure 10(b) for a two-filament wall, to  $\sim 0.4\%$  for a four-filament wall in  
 448 Figure 12(b)). The resultant strains after applying the corrections for the y-direction-based restraint  
 449 coefficient  $\psi_y$  (Equation 2.6) are shown in Figure 12(c). Consequently, the resulting normalized strain  
 450 profiles  $\varepsilon_{zy} = \varepsilon_{free-3D}$  converged to a value close to 1%, consistent with the results shown earlier for  
 451 the same mixture ( $L_{30}$ ) after applying the corrections for restraint in the longitudinal direction alone for a  
 452 single filament wall. This convergence validates the robustness of the proposed analytical model and  
 453 emphasizes once again that, when the geometric restraints are appropriately removed, the remaining  
 454 shrinkage strain reflects the material's intrinsic early-age volume change response governed by binder  
 455 composition and exposure conditions.

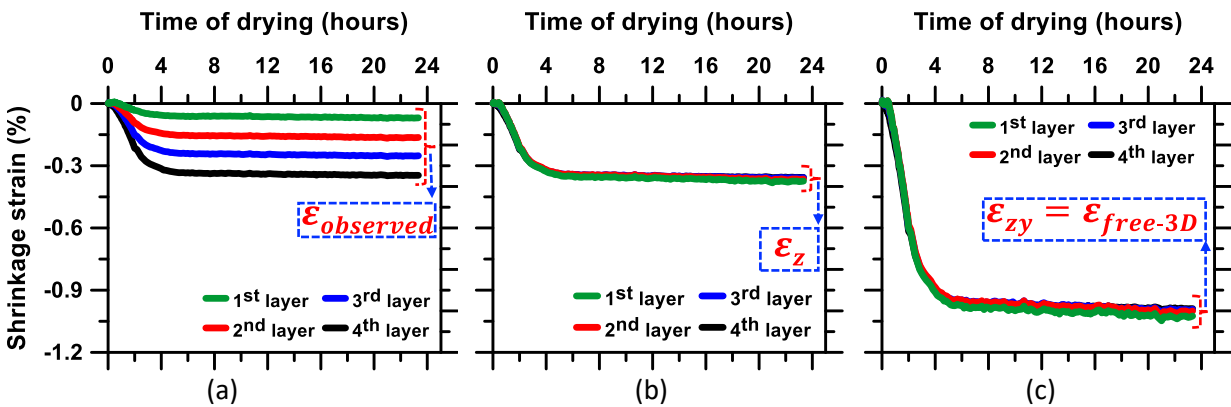


Figure 12: Shrinkage strain profiles for a four-filament wall made using  $L_{30}$  mixture: (a) at various layer heights, (b) after z-direction restraint correction, and (c) after both z- and y-direction restraint correction). Replicate measurements within 8% of each other.

456

457 Figure 13 shows an extended validation of the restraint correction framework through a six-filament, six-  
 458 layer wall printed with the  $L_{30}$  mixture using a 20-mm square nozzle. Strain evolution at the mid-thickness  
 459 of each individual layer over a period of 24 h is shown in Figure 13(a), which shows even lower strains  
 460 than a four-filament wall section, further reinforcing the effect of restraint. It also needs to be noted that  
 461 the slope of the primary regime is much lower in this case than a two- or four-filament wall section,  
 462 indicating the effect of restraint in the shrinkage rate (a potential effect of surface area-to-volume ratio,  
 463 a parameter not addressed in detail in this paper), in addition to the total strains. Similar correction  
 464 approaches to account for the longitudinal and lateral restraints were carried out and the resultant strains  
 465 are shown in Figure 13 (b) and (c) respectively. Once again, the maximum free strains converged to a value  
 466 of  $\sim 1.0\%$ , reflecting the intrinsic shrinkage characteristics observed in experiments involving other  
 467 geometries described earlier. This approach shows that the corrected shrinkage strain reflects the intrinsic  
 468 material behavior governed primarily by binder composition and water loss kinetics driven by  
 469 environmental exposure and chemical reactions. The successful validation of shrinkage strains in a six-  
 470 filament, six-layer wall (with different filament width than the earlier cases) also substantiates the  
 471 determination of  $\psi_y$  values where a constant multiplier was used to reduce the free shrinkage with each  
 472 doubling of thickness.

473

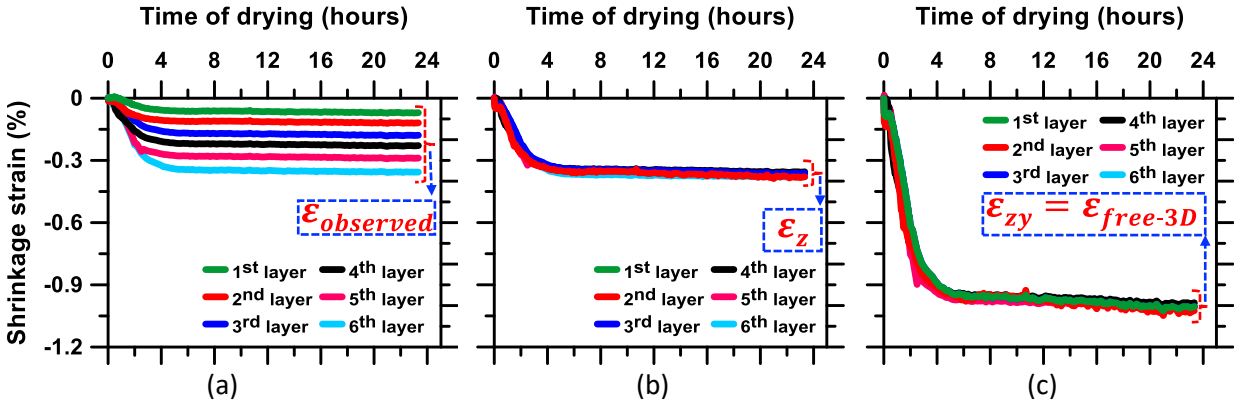


Figure 13: Shrinkage strain profiles for a six filament wall made using  $L_{30}$  mixture: (a) at various layer heights, (b) after z-direction restraint correction, and (c) after both z- and y-direction restraint correction). Quantitative profiles are based on three specimens; measurement variation remained below 6% of the mean.

### 474 3.6. Shrinkage behavior and cracking under severe drying and maximum substrate restraint

475 Figure 14(a) shows the DIC-measured shrinkage strain profile for a single-filament, four-layer wall  
 476 ( $400 \times 30 \times 120$  mm) for the  $L_{30}$  mixture, subjected to forced convection drying. As noted earlier, the  
 477 height-dependent gradient in shrinkage strain arises from longitudinal restraint, and severe drying further  
 478 exacerbates shrinkage strains due to accelerated evaporation (e.g., maximum strains in the layers range  
 479 from  $\sim 1.0\%$  to  $\sim 2.3\%$  under this drying regime, as opposed to  $\sim 0.45\%$  to  $1.0\%$  under the exposure  
 480 condition used in the other experiments reported before in the paper for the single-filament wall of the  
 481 same dimension, made using the  $L_{30}$  mixture). After applying the longitudinal correction (using Equation  
 482 2.4), the strains converged to  $\epsilon_z$ , which in this single-filament case directly represents  $\epsilon_{free-3D}$ , with free  
 483 shrinkage strain of  $\sim 2.3\%$  (Figure 14(b)). Figure 14(c) shows the DIC-derived average longitudinal strain  
 484 fields for different layers, revealing pronounced concentration in the bottom-most filament, consistent  
 485 with substrate induced restraint. This localized concentration coincides with the zone of maximum  
 486 z-direction restraint and correlates with the appearance of first crack, as depicted in Figure 14(d). Figure  
 487 14(d) presents the strain distribution in the vicinity of the crack, soon after the crack initiation, showing  
 488 almost zero the longitudinal strain in the crack zone. The layer-averaged strains, though, continue to  
 489 increase after cracking since the regions away from the crack still are subjected to deformations. Crack  
 490 propagation was observed to initiate at the base and propagate upward along the layer build-up direction,  
 491 confirming that early-age cracking is primarily governed by the combination of rapid drying and high  
 492 substrate-induced restraint.

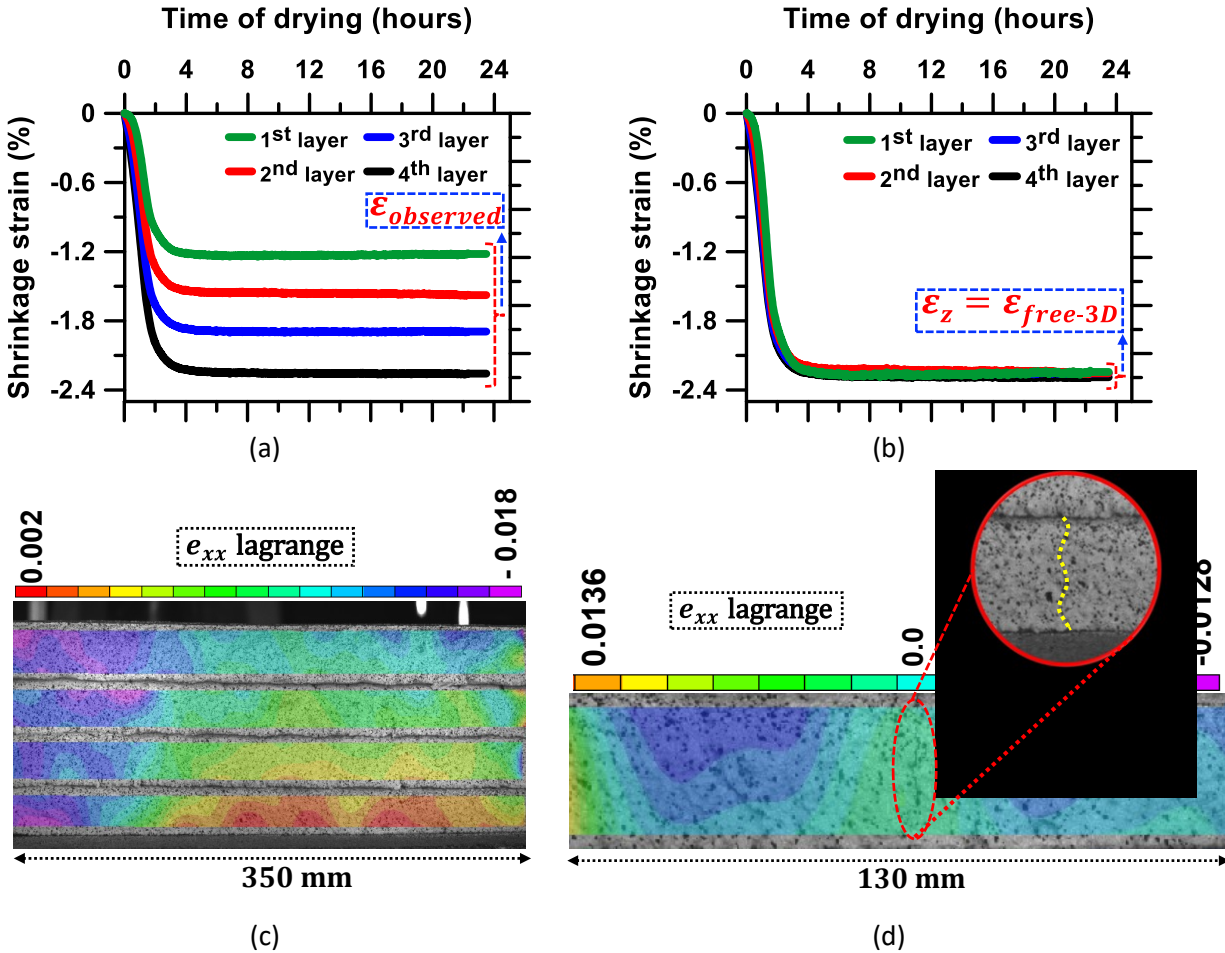


Figure 14: Early-age shrinkage behavior of a single-filament, four-layer wall ( $L_{30}$  mixture) under severe drying: (a) observed strain profiles across the four layers, (b) free strain after z-direction correction, (c) DIC-derived longitudinal strain ( $e_{xx}$ ) distribution across layers at 1.4 h after extrusion, and (d) localized strain distribution in the bottom layer with an inset showing crack initiation and upward propagation along the build-up direction. Replicate measurements within 5% of each other.

493

494 To further elucidate the effects of restraint and cracking, tensile stress development in the layers was  
 495 determined. The elastic modulus development under conditions of accelerated cracking were determined  
 496 using GCT described earlier. Figure 15(a) presents the early-age modulus of elasticity ( $E$ ) as a function of  
 497 drying time. The elastic modulus was obtained by fitting the linear portion of the stress-strain curve  
 498 recorded during GCT, using data from specimens tested at 90, 120, 150, and 180 min. Results from 30 and  
 499 60 min were excluded from this analysis, as the measured moduli were insignificant since they were  
 500 before the initial setting time. Figure 15(b) illustrates the evolution of restrained strain ( $\epsilon_{restrained}$ ) across  
 501 the four layers as a function of time. These restrained strains were computed as the difference between  
 502 observed shrinkage strain ( $\epsilon_{observed}$ ) and free shrinkage strain ( $\epsilon_{free-3D}$ , determined based on the  
 503 procedure described earlier). The restrained strains are plotted only from the time of setting, when the  
 504 material had developed sufficient stiffness to resist deformation. Based on GCT observations and setting

505 time tests, this occurred at  $\sim 1.25$  h (75 min) from mixing, after which tensile stresses were considered to  
506 develop. The evaluation window was limited to 3 h, as cracking occurred within this period.

507 The tensile stresses induced by the accumulated restraint were calculated by multiplying the layer-wise  
508 restraint strains with the corresponding modulus values from GCT ( $\epsilon_{\text{restrained}} \times E$ ), and are shown in  
509 Figure 15(c). Under the imposed severe drying conditions, the first crack was observed in the bottom-  
510 most layer (1<sup>st</sup> layer) at approximately 1.45 h after printing, corresponding to a tensile stress of 0.17 MPa.  
511 Since the average DIC-determined strains in the layer increases with time (even after local strain at the  
512 crack zone drops to zero), increase in average tensile stress with time in the cracked layer is noticed.  
513 Following the first crack, second and third cracks were noticed in the bottom-most layer. The onset of  
514 each crack causes a partial local stress release within the cracked zone, along with strain redistribution to  
515 the adjacent intact zones. While this redistribution mechanism is well established, the DIC analysis focused  
516 on a localized region in the bottom-most layer along the crack path to resolve the immediate post-cracking  
517 strain relaxation, as shown in Figure 14(d). Over time, as drying persisted and material stiffness increased,  
518 the balance between restraint-induced stress and evolving tensile capacity was repeatedly surpassed in  
519 successive layers, leading to progressive upward crack propagation. This sequential failure mechanism  
520 reflects the combined influence of rapid moisture loss, stiffness gains due to hydration, and geometric  
521 restraint from the printed configuration.

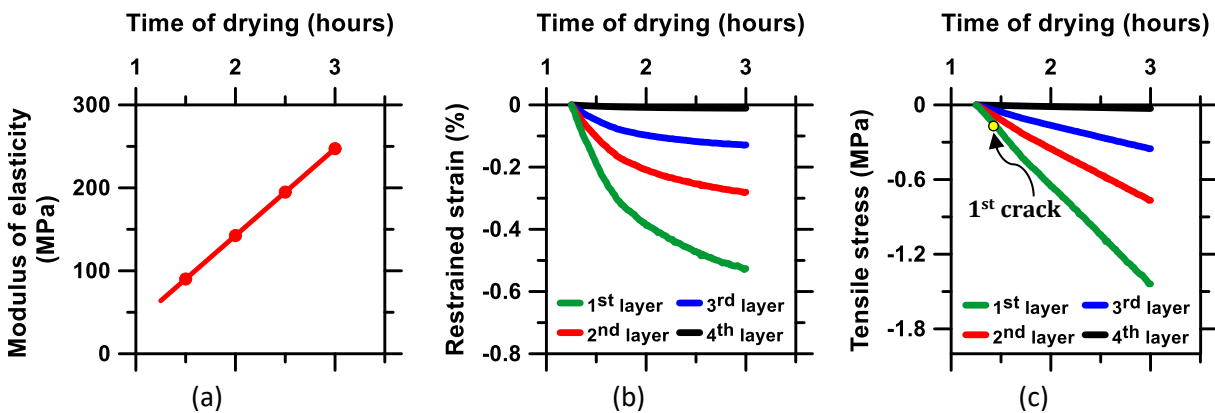


Figure 15: Evolution of: (a) time-dependent modulus of elasticity; measurements at 1.5, 2, 2.5, and 3 h, with the trend extended backward to the mixture's initial setting time, (b) layer-wise average restrained strain evolution over time, and (c) estimated average tensile stress profiles across the layers, for the L<sub>30</sub> mixture.

### 522 3.7. Mitigating substrate restraint by low-friction interlayers

523 Figure 16(a) shows the shrinkage behavior of an identical single-filament, four-layer wall  
524 ( $400 \times 30 \times 120$  mm) printed over a low-friction interface consisting of oiled plastic sheets. For this series,  
525 the uncertainty of the DIC-derived strain estimates was  $\sim 7\%$ . Unlike the previous cases, the strain  
526 distribution across the layers is confined in a narrower range, confirming that reducing substrate friction  
527 effectively lowers z-direction restraint. The strain in the 1<sup>st</sup> layer is significantly higher than in the more  
528 restrained case presented in the earlier experiments, indicating that the wall could deform more freely in  
529 the early plastic stage. While complete elimination of restraint is practically unachievable, the observed  
530 shrinkage profiles approach an ideal free-shrinkage response, with only minor differences between layers

531 due to reduced interfacial resistance. The smaller band of shrinkage profiles suggests that the primary  
532 contributor to early-age restraint in slender 3D-printed walls is the frictional effects at the print bed or at  
533 the completely hardened layer when walls are built up over multiple days.

534 The corresponding DIC-derived horizontal strain field is shown in Figure 16(b), which reveals no  
535 pronounced strain localization near the base filament, in contrast to the severe drying case. Figure 16(c)  
536 presents the optical image of the same specimen after 24 h. No visible cracks are observed in the bottom  
537 filament, which validates the DIC analysis and confirms that reducing substrate friction suppresses  
538 restraint-induced tensile stress and the resulting crack initiation. Although no visible cracking was  
539 observed, microcracking below the DIC resolution and possible layer misalignment from differential free  
540 shrinkage were not investigated here and warrant a separate study.

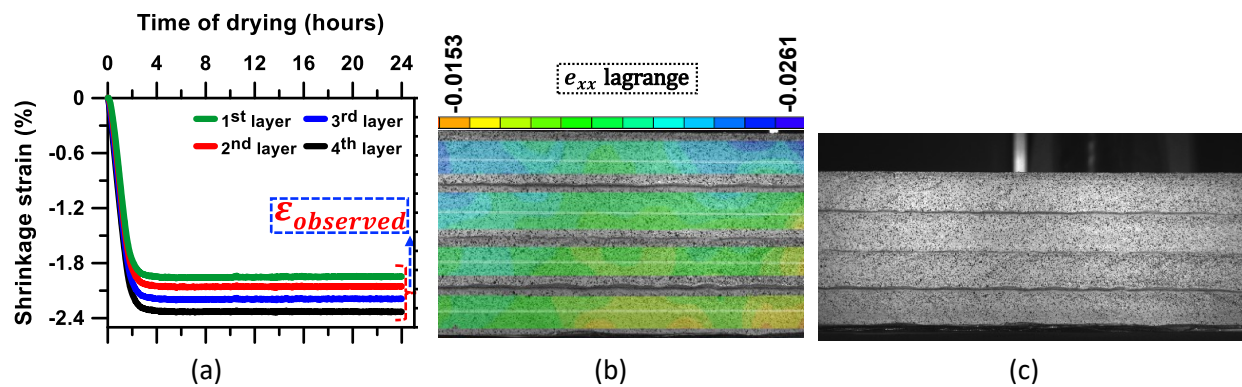


Figure 16: Early-age shrinkage behavior of a single-filament, four-layer wall ( $L_{30}$  mixture) printed over a low-friction substrate: (a) strain profiles measured by DIC across the four layers, (b) DIC-derived longitudinal strain ( $e_{xx}$ ) field across the layers at 3 h after extrusion showing nearly uniform strain distribution with minimal concentration at substrate, and (c) surface image confirming the absence of crack initiation under reduced substrate restraint. Replicate measurements within 7% of each other.

#### 541 4. CONCLUSIONS

542 Early-age shrinkage cracking is a concern for 3D printed concrete structures and is influenced by the  
543 geometry of the printed element (particularly the number of layers and filaments and their dimensions)  
544 and surface roughness of the substrate. The interaction between moisture loss, structural build-up, and  
545 geometric restraint directly affects the time-dependent shrinkage. This study introduces a framework to  
546 characterize early-age shrinkage in 3D printed concrete elements by integrating digital image correlation-  
547 based, layer-specific surface strain measurements and analytical quantifications of geometry-based  
548 restraints. DIC-based measurements of strain starting 24 h from casting were found to be consistent with  
549 measurements obtained using standardized ASTM tests, and thus DIC was used to measure shrinkage  
550 strains starting immediately after printing. The speckling patterns were adjusted before and after the  
551 setting of the mortar to allow for image contrasts but did not influence the measurements. The following  
552 conclusions are obtained from this work:

- 553 1. Early-age surface strains measured by DIC on single- and double filament walls demonstrated the  
554 influence of geometry and surface roughness of the substrate. A rapid increase in strain in the first  
555 few hours (primary regime) was followed by gradual plateauing (secondary regime). The lowest

556 strains were observed on the bottom-most layer in contact with the substrate and the highest strains  
557 in the top-most layer, due to the restraint induced by the substrate. The magnitude of strains was  
558 lower in the multi-filament ( $\geq 2$ ) walls because of the restraint in the lateral direction (y-direction)  
559 also, while the single-filament walls were subjected to only the longitudinal restraint (z-direction).  
560 Surface strains measured using DIC were much lower, and their appearance delayed in thicker, multi-  
561 filament sections because geometric restraint masked the material response, even when moisture  
562 loss conditions were similar.

563 2. An analytical framework was developed to quantify the restraint effects in the longitudinal and lateral  
564 directions as a function of the geometry. A two-stage methodology—first determining the  
565 longitudinal restraint and correcting the measured strains using this parameter and then  
566 implementing the lateral restraint correction—was used. For single-filament walls, only the first stage  
567 is necessary. The time-dependent free shrinkage strains thus obtained are only dependent on the  
568 mixture design (binder components, w/b, and any other additives) and exposure conditions.

569 3. The framework was validated using walls printed using different materials, multiple layers and  
570 filaments, and different element dimensions. The validation effort also enabled the verification of a  
571 few simplifying, yet mechanistically consistent assumptions that were used in the formulations of the  
572 restraint coefficients.

573 4. The influence of evaporation rate and substrate friction were also evaluated. The tensile stress  
574 development was calculated using residual strains (the difference between DIC-measured strains and  
575 analytically calculated free strains) and time-dependent elastic modulus determined using green  
576 compression tests on cylinders cored from the printed walls. Cracks initiated at the layer in contact  
577 with the substrate and propagated along the height as drying progressed. Reducing the friction at the  
578 substrate significantly reduced the vertical restraint, producing nearly uniform layer-wise strains and  
579 enabling the base-layer response to approach the free shrinkage. This suggested that substrate  
580 friction is the primary source of early restraint in slender prints and that its mitigation suppresses  
581 restraint-induced tensile stress and cracking.

582 The framework proposed here helps accurately interpret differential shrinkage in 3D printed concrete  
583 elements. This allows for reliable assessment of binder performance and supports the development of  
584 mixture designs that mitigate the risk of shrinkage-induced cracking. This approach can also be used to  
585 quantify the restraint effects as a function of geometry. The methodology can also support the  
586 development of models for restraint-induced tensile stresses and the potential for shrinkage cracking in  
587 3D-printed structures. Note that the current model assumes near-perfect interfacial bonding and does  
588 not capture deformation occurring during deposition/printing, especially when printing under severe  
589 exposure conditions that impose significant deformations. Accordingly, the derived restraint coefficients  
590 may need to be revised where bonding is deficient or printing-induced strains are significant.

## 591 **Acknowledgement**

592 The authors sincerely acknowledge support from the National Science Foundation (NSF) through Grant  
593 No. OISE 2020095 towards the conduct of this project. The cement and fly ash used in this work was

594 supplied by Salt River Materials Group (Phoenix Cement), the limestone by Omya™, and Type IP cement  
595 by Ash Grove Cement. We acknowledge the use of experimental facilities within the Center for Carbon-  
596 Efficient and Advanced Manufacturing of Materials and Structures (CAMMS) at Arizona State University.

#### 597 **Declaration of competing interest**

598 The authors declare that they have no known competing financial interests or personal relationships that  
599 could have appeared to influence the work reported in this paper.

#### 600 **Data availability**

601 Data will be made available on request.

#### 602 **5. REFERENCES**

603 [1] N. Labonnote, A. Rønquist, B. Manum, and P. Rüter, "Additive construction: State-of-the-art,  
604 challenges and opportunities," *Autom Constr*, vol. 72, pp. 347–366, Dec. 2016, doi:  
605 10.1016/J.AUTCON.2016.08.026.

606 [2] R. A. Buswell *et al.*, "A process classification framework for defining and describing Digital  
607 Fabrication with Concrete," *Cem Concr Res*, vol. 134, p. 106068, Aug. 2020, doi:  
608 10.1016/J.CEMCONRES.2020.106068.

609 [3] D. Liu, Z. Zhang, X. Zhang, and Z. Chen, "3D printing concrete structures: State of the art,  
610 challenges, and opportunities," *Constr Build Mater*, vol. 405, p. 133364, Nov. 2023, doi:  
611 10.1016/J.CONBUILDMAT.2023.133364.

612 [4] R. A. Buswell, W. R. Leal de Silva, S. Z. Jones, and J. Dirrenberger, "3D printing using concrete  
613 extrusion: A roadmap for research," Oct. 01, 2018, *Elsevier Ltd.* doi:  
614 10.1016/j.cemconres.2018.05.006.

615 [5] S. Ghourchian, M. Wyrzykowski, M. Plamondon, and P. Lura, "On the mechanism of plastic  
616 shrinkage cracking in fresh cementitious materials," *Cem Concr Res*, vol. 115, pp. 251–263, Jan.  
617 2019, doi: 10.1016/J.CEMCONRES.2018.10.015.

618 [6] M. Kayondo, R. Combrinck, and W. P. Boshoff, "State-of-the-art review on plastic cracking of  
619 concrete," *Constr Build Mater*, vol. 225, pp. 886–899, Nov. 2019, doi:  
620 10.1016/J.CONBUILDMAT.2019.07.197.

621 [7] G. M. Moelich, J. Kruger, and R. Combrinck, "Plastic shrinkage cracking in 3D printed concrete,"  
622 *Compos B Eng*, vol. 200, p. 108313, Nov. 2020, doi: 10.1016/J.COMPOSITESB.2020.108313.

623 [8] G. M. Moelich, P. J. Kruger, and R. Combrinck, "A plastic shrinkage cracking risk model for 3D  
624 printed concrete exposed to different environments," *Cem Concr Compos*, vol. 130, p. 104516,  
625 Jul. 2022, doi: 10.1016/J.CEMCONCOMP.2022.104516.

626 [9] S. Markin, R. Combrinck, and V. Mechtcherine, "Specifics of plastic shrinkage in 3D-printed  
627 concrete elements," *Cem Concr Res*, vol. 184, p. 107512, Oct. 2024, doi:  
628 10.1016/J.CEMCONRES.2024.107512.

- 629 [10] S. Markin and V. Mechtcherine, "Quantification of plastic shrinkage and plastic shrinkage cracking  
630 of the 3D printable concretes using 2D digital image correlation," *Cem Concr Compos*, vol. 139, p.  
631 105050, May 2023, doi: 10.1016/J.CEMCONCOMP.2023.105050.
- 632 [11] M. K. Mohan, A. V. Rahul, G. De Schutter, and K. Van Tittelboom, "Extrusion-based concrete 3D  
633 printing from a material perspective: A state-of-the-art review," *Cem Concr Compos*, vol. 115,  
634 Jan. 2021, doi: 10.1016/j.cemconcomp.2020.103855.
- 635 [12] D. S. Kurup, M. K. Mohan, K. Van Tittelboom, G. De Schutter, M. Santhanam, and A. V. Rahul,  
636 "Early-age shrinkage assessment of cementitious materials: A critical review," *Cem Concr*  
637 *Compos*, vol. 145, p. 105343, Jan. 2024, doi: 10.1016/J.CEMCONCOMP.2023.105343.
- 638 [13] J. Van Der Putten, D. Snoeck, R. De Coensel, G. De Schutter, and K. Van Tittelboom, "Early age  
639 shrinkage phenomena of 3D printed cementitious materials with superabsorbent polymers,"  
640 *Journal of Building Engineering*, vol. 35, p. 102059, Mar. 2021, doi: 10.1016/J.JOBE.2020.102059.
- 641 [14] R. J. M. Wolfs, F. P. Bos, and T. A. M. Salet, "Early age mechanical behaviour of 3D printed  
642 concrete: Numerical modelling and experimental testing," *Cem Concr Res*, vol. 106, pp. 103–116,  
643 Apr. 2018, doi: 10.1016/J.CEMCONRES.2018.02.001.
- 644 [15] H. Zhang, L. Hao, S. Zhang, J. Xiao, and C. S. Poon, "Advanced measurement techniques for plastic  
645 shrinkage and cracking in 3D-printed concrete utilising distributed optical fiber sensor," *Addit*  
646 *Manuf*, vol. 74, p. 103722, Jul. 2023, doi: 10.1016/J.ADDMA.2023.103722.
- 647 [16] X. Han, J. Yan, T. Chen, B. Tang, and Y. Lin, "Plastic shrinkage of 3D printed concrete under  
648 different self-weight of upper layers," *Constr Build Mater*, vol. 399, p. 132564, Oct. 2023, doi:  
649 10.1016/J.CONBUILDMAT.2023.132564.
- 650 [17] S. Markin, J. A. L. Cordova, R. Combrinck, and V. Mechtcherine, "Deformation behaviour of 3D-  
651 printed concrete elements induced by plastic shrinkage," *Constr Build Mater*, vol. 449, p. 138073,  
652 Oct. 2024, doi: 10.1016/J.CONBUILDMAT.2024.138073.
- 653 [18] E. D. Dzaye, E. Tsangouri, K. Spiessens, G. De Schutter, and D. G. Aggelis, "Digital image  
654 correlation (DIC) on fresh cement mortar to quantify settlement and shrinkage," *Archives of Civil*  
655 *and Mechanical Engineering*, vol. 19, no. 1, pp. 205–214, Mar. 2019, doi:  
656 10.1016/J.ACME.2018.10.003/METRICS.
- 657 [19] P. Zhao, A. M. Zsaki, and M. R. Nokken, "Using digital image correlation to evaluate plastic  
658 shrinkage cracking in cement-based materials," *Constr Build Mater*, vol. 182, pp. 108–117, Sep.  
659 2018, doi: 10.1016/J.CONBUILDMAT.2018.05.239.
- 660 [20] Y. Shi *et al.*, "Early-age inhomogeneous deformation of 3D printed concrete: Characteristics and  
661 influences of superplasticizer and water-binder ratio," *Journal of Building Engineering*, vol. 86, p.  
662 108956, Jun. 2024, doi: 10.1016/J.JOBE.2024.108956.
- 663 [21] M. Weisbrich, D. Messerer, and K. Holschemacher, "Measurement of early age deformations in  
664 cement-based materials using distributed fiber optic sensors," *Cem Concr Compos*, vol. 165, p.  
665 106353, Jan. 2026, doi: 10.1016/J.CEMCONCOMP.2025.106353.

- 666 [22] I. M. G. Bertelsen, C. Kragh, G. Cardinaud, L. M. Ottosen, and G. Fischer, "Quantification of plastic  
667 shrinkage cracking in mortars using digital image correlation," *Cem Concr Res*, vol. 123, p.  
668 105761, Sep. 2019, doi: 10.1016/J.CEMCONRES.2019.05.006.
- 669 [23] S. Markin, J. A. L. Cordova, and V. Mechtcherine, "Evolution of capillary pressure in 3D-printed  
670 concrete elements: numerical modelling and experimental validation," *Constr Build Mater*, vol.  
671 409, p. 133677, Dec. 2023, doi: 10.1016/J.CONBUILDMAT.2023.133677.
- 672 [24] L. Ma *et al.*, "Water loss and shrinkage prediction in 3D printed concrete with varying w/c and  
673 specimen sizes," *Cem Concr Compos*, vol. 149, p. 105523, May 2024, doi:  
674 10.1016/J.CEMCONCOMP.2024.105523.
- 675 [25] E. D. Dzaye, E. Tsangouri, G. De Schutter, and D. G. Aggelis, "Full-Field Settlement Measurement  
676 at Fresh Cementitious Material by Digital Image Correlation," *Journal of Advanced Concrete  
677 Technology*, vol. 17, no. 4, pp. 168–176, Apr. 2019, doi: 10.3151/JACT.17.168.
- 678 [26] S. A. O. Nair, S. Panda, M. Santhanam, G. Sant, and N. Neithalath, "A critical examination of the  
679 influence of material characteristics and extruder geometry on 3D printing of cementitious  
680 binders," *Cem Concr Compos*, vol. 112, p. 103671, Sep. 2020, doi:  
681 10.1016/J.CEMCONCOMP.2020.103671.
- 682 [27] S. A. O. Nair, H. Alghamdi, A. Arora, I. Mehdipour, G. Sant, and N. Neithalath, "Linking fresh paste  
683 microstructure, rheology and extrusion characteristics of cementitious binders for 3D printing,"  
684 *Journal of the American Ceramic Society*, vol. 102, no. 7, pp. 3951–3964, Jul. 2019, doi:  
685 10.1111/JACE.16305.
- 686 [28] S. Das, A. Kizilkanat, and N. Neithalath, "Crack propagation and strain localization in metallic  
687 particulate-reinforced cementitious mortars," *Mater Des*, vol. 79, pp. 15–25, Aug. 2015, doi:  
688 10.1016/J.MATDES.2015.04.038.
- 689 [29] D. Zhang, C. D. Eggleton, and D. D. Arola, "Evaluating the mechanical behavior of arterial tissue  
690 using digital image correlation," *Experimental Mechanics* 2002 42:4, vol. 42, no. 4, pp. 409–416,  
691 Dec. 2002, doi: 10.1007/BF02412146.
- 692 [30] A. Tripathi, S. A. O. Nair, and N. Neithalath, "A comprehensive analysis of buildability of 3D-  
693 printed concrete and the use of bi-linear stress-strain criterion-based failure curves towards their  
694 prediction," *Cem Concr Compos*, vol. 128, p. 104424, Apr. 2022, doi:  
695 10.1016/J.CEMCONCOMP.2022.104424.
- 696 [31] S. Afroz, Q. D. Nguyen, Y. Zhang, T. Kim, and A. Castel, "Cracking of limestone calcined clay  
697 blended concrete and mortar under restrained shrinkage," *Constr Build Mater*, vol. 386, p.  
698 131599, Jul. 2023, doi: 10.1016/J.CONBUILDMAT.2023.131599.
- 699 [32] M. Wyrzykowski, C. Di Bella, D. Sirtoli, N. Toropovs, and P. Lura, "Plastic shrinkage of concrete  
700 made with calcined clay-limestone cement," *Cem Concr Res*, vol. 189, p. 107784, Mar. 2025, doi:  
701 10.1016/J.CEMCONRES.2025.107784.
- 702 [33] C. Varhen, I. Dilonardo, R. C. de Oliveira Romano, R. G. Pileggi, and A. D. de Figueiredo, "Effect of  
703 the substitution of cement by limestone filler on the rheological behaviour and shrinkage of

- 704 microconcretes,” *Constr Build Mater*, vol. 125, pp. 375–386, Oct. 2016, doi:  
705 10.1016/J.CONBUILDMAT.2016.08.062.
- 706 [34] J. M. Khatib, R. Ramadan, H. Ghanem, A. Elkordi, and M. Sonebi, “Effect of limestone fines as a  
707 partial replacement of cement on the chemical, autogenous, drying shrinkage and expansion of  
708 mortars,” *Mater Today Proc*, vol. 58, pp. 1199–1204, Jan. 2022, doi:  
709 10.1016/J.MATPR.2022.01.336.
- 710 [35] Y. Briki, M. Zajac, M. Ben Haha, and K. Scrivener, “Impact of limestone fineness on cement  
711 hydration at early age,” *Cem Concr Res*, vol. 147, p. 106515, Sep. 2021, doi:  
712 10.1016/J.CEMCONRES.2021.106515.
- 713 [36] K. De Weerd, M. Ben Haha, G. Le Saout, K. O. Kjellsen, H. Justnes, and B. Lothenbach, “Hydration  
714 mechanisms of ternary Portland cements containing limestone powder and fly ash,” *Cem Concr  
715 Res*, vol. 41, no. 3, pp. 279–291, Mar. 2011, doi: 10.1016/j.cemconres.2010.11.014.
- 716 [37] G. M. Moelich, P. J. Kruger, and R. Combrinck, “The effect of restrained early age shrinkage on  
717 the interlayer bond and durability of 3D printed concrete,” *Journal of Building Engineering*, vol.  
718 43, p. 102857, Nov. 2021, doi: 10.1016/J.JOBE.2021.102857.
- 719 [38] H. Zhang and J. Xiao, “Plastic shrinkage and cracking of 3D printed mortar with recycled sand,”  
720 *Constr Build Mater*, vol. 302, p. 124405, Oct. 2021, doi: 10.1016/J.CONBUILDMAT.2021.124405.
- 721 [39] V. Mechtcherine, V. N. Nerella, F. Will, M. Näther, J. Otto, and M. Krause, “Large-scale digital  
722 concrete construction – CONPrint3D concept for on-site, monolithic 3D-printing,” *Autom Constr*,  
723 vol. 107, p. 102933, Nov. 2019, doi: 10.1016/J.AUTCON.2019.102933.
- 724 [40] J. Cai, J. S. Wang, Q. Zhang, C. Du, M. Meloni, and J. Feng, “State-of-the-art of mechanical  
725 properties of 3D printed concrete,” *Case Studies in Construction Materials*, vol. 21, p. e03847,  
726 Dec. 2024, doi: 10.1016/J.CSCM.2024.E03847.
- 727